

Reconstructing Time-of-Flight Detector Values of Angular Streaking Using Machine Learning

David Meier, Jens Viefhaus, and Gregor Hartmann
*Helmholtz-Zentrum für Materialien und Energie GmbH,
Albert-Einstein-Straße 15, 12489 Berlin, Germany*

Wolfram Helml
*Zentrum für Synchrotronstrahlung, Technische
Universität Dortmund, 44227 Dortmund, Germany*

Thorsten Otto
*Deutsches Elektronen-Synchrotron DESY,
Notkestr. 85, 22607 Hamburg, Germany*

Bernhard Sick
*Intelligent Embedded Systems, University of Kassel,
Wilhelmshöher Allee 73, 34121 Kassel, Germany*

(AIM-ED – Joint Lab Helmholtz-Zentrum für Materialien
und Energie, Berlin (HZB) and University of Kassel)

(Dated: January 16, 2025)

Abstract

Angular streaking experiments enable for experimentation in the attosecond regions. However, the deployed time-of-flight (TOF) detectors are susceptible to noise and failure. These shortcomings make the outputs of the TOF detectors hard to understand for humans and further processing, such as for example the extraction of beam properties. In this article, we present an approach to remove high noise levels and reconstruct up to three failed TOF detectors from an arrangement of 16 TOF detectors. Due to its fast evaluation time, the presented method is applicable online during a running experiment. It is trained with simulation data, and we show the results of denoising and reconstruction of our method on real-world experiment data.

I. INTRODUCTION

During the last years, the X-ray Free Electron Lasers (XFELs) have been developed and established as a new generation of light source for X-ray experiments [1]. The Linear Accelerator (LINAC) Coherent Light Source (LCLS) located in Stanford, California, is such a light source [2]. XFELs can produce radiation with nearly ten orders of magnitude higher brightness compared to previous light sources. The pulse durations can range from 500 to less than subfemtoseconds ($10^{-15}s$) [3]. This property is beneficial because most experiments performed at XFELs require a short, well-defined photon pulse.

At LCLS, angular streaking experiments are carried out. The main goal of these experiments are measurements in the attosecond ($10^{-18}s$) region. These experiments allow us to gain previously inaccessible knowledge, since some atomic processes happen on this time scale. For example, tunnel ionization is an effect where a particle goes through a potential barrier. A measuring resolution in attoseconds is required to analyze this phenomenon and has successfully been conducted [4]. In angular streaking, X-rays ionize the gas introduced into the chamber through a gas needle for examination. That means that so-called photoelectrons are emitted from this gas. A circularly polarized laser has temporal and spatial overlap with the X-ray pulses in the target gas chamber. The laser's electromagnetic field then streaks the emitted photoelectrons according to their emission time in different angular positions due to the circular polarization of the laser. In our particular experimental setup, the emitted electrons are detected by an angularly aligned array of 16 electron TOF spectrometers set up in the dipole plane, i.e. the plane perpendicular to the incoming X-ray

pulses. The TOF spectrometers are located in steps of 22.5° and are thus covering the entire circle of the dipole plane. For a detailed description on the experimental setup and how the real experiment data have been recorded, please refer to [3].

The TOF spectrometers used in the experiment are highly sensitive, and an unknown number of TOF detectors can break before or during the experiment. They can fail completely or produce implausible results. If they produce implausible results, they are disabled manually. While automating the detection of such events using anomaly detection methods could be a valuable extension, it is not covered within the scope of this study. In addition to frequent failures, the TOF detectors suffer from extremely high noise. Additionally, to avoid saturation, these detectors are restricted in the number of electrons they collect. However, this constraint results in an insufficient sample size for accurate Poisson statistics.

Therefore, we present an approach to reduce noise and reconstruct the information of failed TOF detectors using simulation knowledge and neural networks and demonstrate this approach with real-world data from the experiment at LCLS. For this approach, we train a neural network exclusively on simulated data. This neural network receives the simulated detector images augmented with artificially added noise and deactivated TOF detectors mimicking failed TOF detectors. The neural network is trained to map these noisy, incomplete images to their corresponding noise-free versions with no failed TOF detectors. Since the training data is fully simulated, the ground truth for non-noisy and complete detector images is known, enabling evaluation and refinement of the network’s outputs during the training process.

The main advances provided by the method proposed in the present study are:

A. Fast Denoising of TOF Detector Data

We propose a neural network-based approach for high-noise reduction in detector images, enhancing readability and preparing the data for further automated analysis. This approach is specifically designed for *online* processing, meaning that it adds a maximum delay of one second per data batch. It handles data with batch sizes of at least 1024 detector images in 217.53 ms with 100 threads on an AMD EPYC 7662, allowing it to match with one second data batches at LCLS experiment, which supplies data at a rate of 120 detector images per second. This capability enables near real-time feedback for the experimentator and further

online processing, similar to the retrospective evaluation conducted in [3]. Additionally, extracting characteristics online from the X-ray pulse is possible, as presented in [5] for a similar experiment at European XFEL located in Hamburg, Germany.

B. Fast Reconstruction of Missing TOF Detectors Using Simulation Knowledge

Furthermore, we want to reconstruct missing TOF detectors. We assume that defective TOF detectors either fail completely or have all their channels manually set to zero in the event of incorrect outputs. We will train neural networks that can reconstruct up to three failed TOF detectors. We compare networks trained explicitly for a distinct number of failed TOF detectors with those trained for one up to three failed TOF detectors. This reconstruction capability is also crucial for further processing steps, with our method allowing reconstructions online, as previously defined.

C. Improving Future Designs of TOF Arrays

Because our neural network models are trained only using simulation data, we know which information was left out for reconstruction. Based on the reconstruction quality of our TOF reconstruction approach, we can determine at which points our reconstruction algorithm has difficulties. By that, these TOF arrays presumably have less redundant information. This knowledge can be used to improve future designs of TOF arrays, for example, by having a more significant overlap of specific TOF detectors or by constructing TOF arrays entirely different. For instance, it could be beneficial to use a different geometry, to avoid the loss of too much redundant information if two correlated TOF detectors fail.

II. RELATED WORK

Since the data recorded from the TOF detectors are two-dimensional, we consider them as images in this discussion. In the literature, the task of reconstructing missing parts of images is referred to as *image inpainting*. Typically, parts of the image are distorted or covered, and the distorted or concealed parts should be recovered. One existing method is the simple and fast *coherence transport* [6]. These algorithms are based on nonlinear higher-order partial

differential equations. Nevertheless, these methods are only based on a single image and cannot incorporate knowledge from a simulation or image database. Furthermore, they rely on containing enough information on this single image to recover the missing parts of the image.

More sophisticated approaches incorporating knowledge from image databases containing images from the same domain use Generative Adversarial Networks (GANs). The following summary on the development of GAN approaches is based on [7]. A significant advance was using Convolutional Neural Networks (CNNs) for image inpainting [8, 9]. However, these methods could not distinguish if an input pixel exists in the data or is missing. The approach of using *partial convolution* is a modification that replaces missing input pixels with zeros and normalizes the output depending on the number of valid pixels [10]. This approach, however, relies on manual hardcoded certainty propagation. There exist methods to replace these components by learning them. Nevertheless, they use about half of the network parameters to propagate the certainties through the network [11, 12]. This makes the evaluation of the networks more expensive. Furthermore, GAN-based approaches are hard to train because they typically suffer from mode collapse [13]. Mode collapse means the generator repeatedly produces the same image since it is a plausible output for the discriminator. If the discriminator fails to learn to reject this sample because it is in a local minimum, the generator-discriminator loop is stuck to this image. Moreover, GANs can suffer from vanishing gradients when the discriminator is trained too well [14]. Some of these shortcomings can be mitigated using the so-called Wasserstein-GANs, which uses the Wasserstein metric to measure the distance of the latent variable distribution from a standard normal distribution [14]. However, they are slower in the training process because the Wasserstein distance calculation is computationally more expensive.

More recently, so-called stable diffusion models, initially designed for text-to-image transformations, are used for inpainting tasks [15]. Stable diffusion methods start with a randomly generated two-dimensional noise. Then, this image is denoised iteratively with a previously trained decoder. The approach presented in [15] uses the incomplete image as input. Noise is added to both the already existing and missing parts. This image is denoised by the diffusion model. After this step, the next iteration starts, but instead of taking noise to inpaint the missing parts, the denoised output of the diffusion model is used for inpainting. Even though these models currently show the best results in the inpainting of natural images, we

will not use diffusion models since they rely on repeated application of the decoders, making their use too slow and thus intractable for online experimentation applications.

Other techniques used for inpainting tasks are fully-connected or Convolutional Autoencoder (CAE) [16]. An autoencoder is a neural network consisting of two parts: The encoder is composed of several layers with decreasing size. The last layer of this encoder is called bottleneck, and its neuron count is called bottleneck size. The second part, the decoder, typically has the same amount of layers but with symmetrically increasing layer sizes. Usually, one trains an autoencoder to reconstruct the input data precisely. This procedure allows us to learn a compressed representation of the input data using the encoder and enables the decoder to unfold the data. Autoencoders provide fast and accurate reconstructions. For autoencoders, extensions exist for taking the circular setup of the TOF detectors into account [17]. These so-called Circular Convolutional Neural Networks (CCNNs) replace the zero padding from the convolution layers in the encoder by a circular padding. This means that the left-side pixels are padded with values from the right side edge of the input and the right-side pixels are padded with values from the left-side edge. For the transposed convolution layers in the decoder the CCNNs add padding to their input and cut the outputs than accordingly to their expected output shapes.

As previously described, GANs exhibit significant challenges during training, and diffusion models are too slow for our intended online application. Due to this difficulties, fully-connected and convolutional autoencoders—also with the addition of circular padding—emerge as the most promising approaches. Therefore, this study will focus on evaluating and comparing these autoencoder methods.

To achieve the advances discussed in Sec. I, we need to overcome some largely unexplored challenges. First, we need to investigate ways to transfer knowledge from simulation data to real-world data. Additionally, it is important to avoid overfitting on the simulation, and thus ensure that the resulting model is still general enough to be applied to the real data. Finally, we need to address how we can mitigate the disproportionately negative impact of certain failed TOF detectors on overall reconstruction quality.

III. METHOD

A. Simulation & Dataset

Using the publicly available (https://github.com/hz-b/tof-reconstruction/blob/main/data_generation.py) partial-wave-based simulation by Hartmann *et al.*, we generate detector images similar to those recorded during the experiments. Figure 1 shows an example of such a detector image on the right. We will use these detector images later to train the neural networks, because the images generated in this way have the advantage that they are without unknown noise and complete, i.e. the complete data of all TOFs are shown. These detector images consist of 16 TOF angles and 60 discrete equidistant kinetic energy steps, respectively. The color shows the intensity, which means the number of electrons per energy level observed at the angularly distributed TOF detectors.

The simulation first generates random spectrograms to create these detector images. A spectrogram, as shown on the left side of Fig. 1, represents the time–energy distribution of the X-ray pulses. In Fig. 1, it contains three broad intensity peaks. Even though these spectrograms cannot be measured in real-world experiments, they visually represent the most significant properties of the X-ray pulses. These properties can only be inferred indirectly through the resulting detector images. The generated spectrograms are the sum of 1–5 two-dimensional Gaussian distributions, referred to as peaks in Tab. I. The variance of these distributions is randomly chosen from a uniform distribution $\mathcal{U}(0, \sigma_{\max})$, denoted as the number of phase steps, one step equals $\frac{35}{80}$ femtoseconds for the used laser.

The simulation translates this spectrograms to detector images, by imitating the streaking effects of the circularly polarized laser on the photoelectrons in different angular positions due to their emission time. Since this emission is induced by the X-ray pulses, and the circularly polarized laser is synchronized with the X-ray pulses, the peaks from the spectrogram produce the waves on the detector images: The top peak in the spectrogram produces the top wave in the detector image. The left intensity peak at around 20 time steps produces the broader high intensity wave in the middle on the detector image. The right high intensity peak produces the other wave in the middle of the detector image, showing that their produced waves can also overlap each other. It is also visible that a phase shift (displacement in time axis) results in a displacement of the TOF position of the wave and a shift

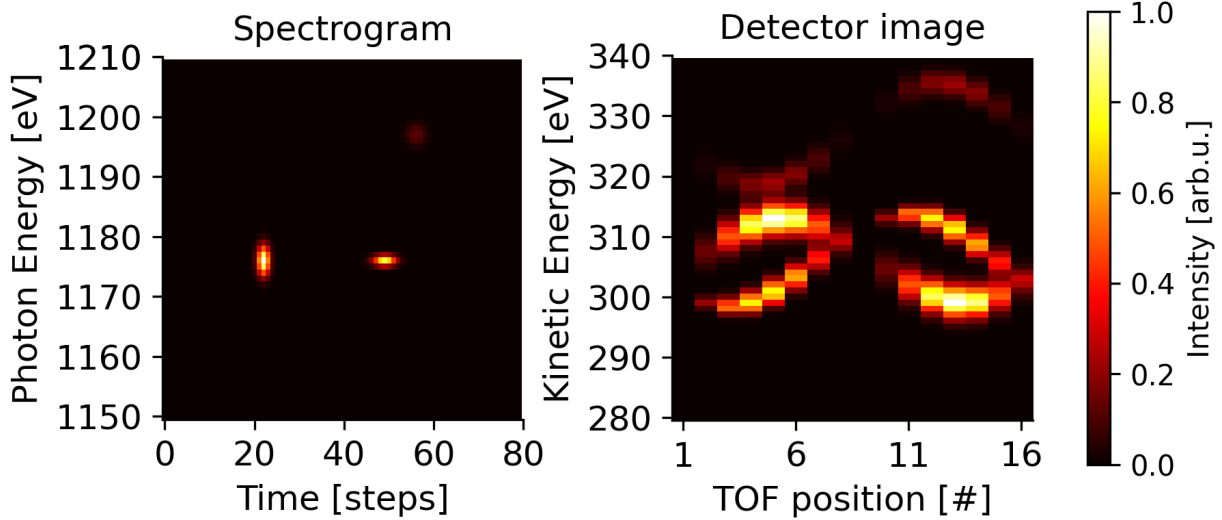


FIG. 1. The simulation generates random spectrograms (left) and translates them to the detector images (right).

in photon energy results in a displacement in the kinetic energy axis of the detector image. The remaining parameters listed in Tab. I are the settings of the detector setup.

The ellipticity of the polarization laser at some phase step ϕ is calculated with the following ellipticity function:

$$\text{ef}(\phi) = \frac{\varepsilon^2}{(\varepsilon \cos(\phi - \theta))^2 + (\sin(\phi - \theta))^2} \quad (1)$$

The ellipticity ε describes how closely the polarization of the laser approaches circularity, while the ellipse tilt angle θ represents the orientation of the polarization ellipse. These values have been measured for this experiment [3].

The translation from spectrograms \mathbf{S} to detector images \mathbf{D} works as follows:

$$d_{ij} = \sum_{i,j=0}^{i=80,j=60} \text{sim} \left(j, \kappa, \frac{2\pi i}{80} \right) s_{ij} \quad (2)$$

The values d_{ij} and s_{ij} are the entries of the according spectrogram \mathbf{S} and the resulting detector image \mathbf{D} . The kick κ is the amplitude of the waves, i.e. the maximum streaking amplitude of the electrons induced by the streaking laser [5]. It is drawn from a uniform

parameter	value
peak	[1, ..., 5]
σ_{\max}	7 steps
kick κ	[0, 100] eV
ellipticity ε	0.73
ellipse tilt θ	$\frac{3}{8}\pi$ rad
β_2	2

TABLE I. Parameters and intervals of simulation.

distribution $\kappa \sim \mathcal{U}(0, 100)$ for enabling unbiased training, since the kick can vary for every pulse.

The simulation of a partial wave is calculated as follows:

$$\text{sim}(e_{\text{kin}}, \kappa, \phi) = I_{\text{electron}} \cdot g(e_{\text{kin}}, \text{sine}(e_{\text{kin}}, \kappa, \phi), \sigma_E)^\top \quad (3)$$

We set $\sigma_E = 1\text{eV}$ as the standardized width of the Gaussian curves, matching the energy step size in the detector images. This choice ensures that any realistic partial waves for the detector image can be constructed.

The angular distribution I_{electron} is calculated with the following equation [3, 18]:

$$I_{\text{electron}} = \frac{\beta_2}{4} (1 - \cos(2\alpha)) \quad (4)$$

The anisotropy angular distribution parameter β_2 modulates the shape of the photoelectron angular distribution and is characteristic of the orbital of the target gas. We set $\beta_2 = 2$ because the s-orbital of neon gas is being excited.

The mathematical representation of all 16 TOF detector angles in the dipole plane is denoted with α .

The function g is approximating the Gaussian function with full width half maximum:

$$g(x, x_0, x_w) = \exp\left(-\frac{(x - x_0)^2}{2\left(\frac{x_w}{2.35}\right)^2}\right) \quad (5)$$

While x is the independent variable for which the Gaussian function is evaluated, x_0 is the peak position of the Gaussian curve, x_w is the width of the Gaussian curve at half of its maximum height.

The sine determines the peak position of the Gaussian curve:

$$\text{sine}(e_{\text{kin}}, \kappa, \phi) = e_{\text{kin}} + \kappa + \cos(\alpha - \phi) \text{ef}(\phi) \quad (6)$$

By running the simulation – generating random spectrograms and translating them to detector images – 6 million times, the dataset for the experiments in this article is created. It is stratified by the amount of peaks, thus it contains an equal amount of samples with one to five peaks each. The number of peaks in the dataset is shuffled to prevent bias in the training process. For training, we split this dataset into 4.8 million training and 600 000 validation samples. Due to the high amount of required evaluations for the following examinations, we limited the test data to 100 000 samples. Training data is used by the neural network during training, and the validation dataset is used to assess a stopping point for training. The test dataset is not used during training and is utilized for the final evaluation of the trained models.

B. Noise & Data Augmentation

We incorporate different forms of artificial noise into the simulation outputs for our denoising and reconstruction method, aiming to imitate the noise of the actual TOF detectors as realistically as possible. Due to the experiment’s design, noise levels are unpredictable and can vary significantly across experiments. The detector’s noise can be categorized into signal-dependent and signal-independent noise.

The signal-dependent noise increases with the intensity potentially non-linearly and can have electric or physical sources, such as secondary particles or multi-photon effects. Since the variability in noise across different experiments prevents a consistent estimation, we account for this type of noise with high-intensity peak noise in the dataset and training. We model it as a uniformly distributed random variable to avoid assumptions about the noise magnitude.

The signal-independent noise is a white detector noise that is relatively higher for weaker intensities. We address this noise with a Gaussian noise with uniformly distributed variance. Additionally, due to TOF detector calibration, saturation effects can be ruled out for our experiment. In Appendix B, showing that the total measured electron intensities by all TOF detectors correlate nearly linearly with the total electron intensity measured by a gas

monitor detector, rather than transitioning to a flattened curve.

For training, we add noise to the detector images with disabled TOF detectors as input and the denoised complete detector image as target. Please note that the order of the following modifications is important. We choose all parameters such that the noise level of the created detector image is visually higher than in the recorded image at the real machine.

1. **Dataset High-Intensity Peaks:** During dataset creation, we simulate 1-15 random single pixels of high intensity by adding random, uniformly distributed single pixel spots to the spectrogram. The intensity of these pixels is also random, uniformly distributed. These peaks create isolated, high-intensity spots in the detector images, mimicking spikes as shown in Hartmann *et al.* Figure 2c [3].
2. **Training High-Intensity Peaks:** To create this noise, we set a probability p_{peak} to which every pixel of a TOF detector is set to the maximum value of the detector image. We choose the maximum value, so that it imitates a high intensity noise peak. In a later step, we add Gaussian noise to the entire detector image, so that the Gaussian noise is also applied to the high peaks making the simulated detector images more realistic and harder to detect by the denoising mechanism. For the high-intensity peak noise, we generate a matrix \mathbf{P} with equally distributed random values as shown in the following equation:

$$p_{ij} \sim \mathcal{U}(0, 1). \quad (7)$$

This matrix has the same size as the detector images $i \times j$, where $i \in \{1, \dots, 16\}$ is the TOF detector position and $j \in \{1, \dots, 60\}$ is the amount of energy steps, which corresponds to the resolution of the TOF detectors.

If an entry p_{ij} is less or equal to p_{peak} , it is set to the maximum value of the current detector image as follows:

$$\bar{x}_{ij} = \begin{cases} x_{ij}, & \text{if } p_{ij} \leq p_{\text{peak}} \\ \max_{kl} (x_{kl}), & \text{else.} \end{cases} \quad (8)$$

3. **Normalization:** Next, we min-max normalize the detector images. We apply the normalization individually per image. The real-world images are also normalized per

Model	Training Data
1TOF, 2TOF, 3TOF	Disable 1, 2 or 3 random TOF detectors respectively
General	Disable 1–3 TOF detectors randomly
Spec	Disable the TOF detectors at positions #8 and #13
Mean	No data; Calculates means only from neighboring TOF detectors

TABLE II. Different models trained with varying datasets adapted for specific purposes.

image since only the relative differences per image should be considered, given the technical functionality of TOF detectors.

4. **Gaussian Noise:** It is important that the previous normalization step is performed first, ensuring that the Gaussian noise is added to the normalized values, as illustrated in the following equation:

$$\tilde{x}_{ij} = \bar{x}_{ij} + p_{ij} \quad (9)$$

The variables i and j are chosen similar to Eq. (7). The entries of the random matrix \mathbf{P} are drawn from a Gaussian distribution:

$$p_{ij} \sim \mathcal{N}(0, \sigma^2) \quad (10)$$

The noise level can be chosen by setting σ which is the standard deviation of the Gaussian distribution. We choose a random noise level of $\sigma \sim \mathcal{U}(0, 0.2)$, so that the noised images look as similar as possible to the real images.

5. **Detector disablement:** The next step is to disable the TOF detectors, with specific methods applied for training each model, as listed in Tab. II. In the following, '#' denotes a TOF detector's position, while a number before TOF detectors indicates the count of uniformly random-selected TOF detectors. The selection strategy of which TOF detectors to disable is shown in detail in Alg. 1. The first TOF detector is selected randomly. All others are picked randomly as well, or, with probability ξ , a neighboring or opposite TOF detector is chosen for disabling if possible.
6. **Normalization:** Min-max normalization is applied to each image individually again, ensuring that the values of the detector images—captured with disabled TOF

detectors—are rescaled between zero and one. This normalization process can also be implemented in real-world scenarios where TOF detector failures occur. This approach remains valid since we focus on the time-energy structure rather than the beam intensity. Furthermore, as demonstrated in Appendix B, the X-ray photon energies can easily be extracted from the raw data and correlate almost linear with the corresponding values of the gas monitor detector. This correlation enables reconversion of the detector images to their original photon intensity level and thus ensuring no loss of essential information.

In Appendix B, showing that the total measured electron intensities by all TOF detectors correlate nearly linearly with the total electron intensity measured by a gas monitor detector, rather than transitioning to a flattened curve.

As a baseline, we will use the *mean* model: This model averages over the neighbors’ values to replace the values of a missing TOF detector. If a neighbor of a missing TOF detector is also missing, we take the nearest neighbor. Due to the experimental setup’s circular nature, every TOF detector has two neighbors since the first TOF detector is located next to the last. Unlike the other models based on simulation data, this model is entirely data-free, meaning it relies only on information from the neighboring TOF detectors in the current detector image without requiring any training data or pre-computed statistics. By checking if our proposed neural network models have a lower loss value than the mean model, we verify that the neural network models do not only learn to mean over the neighbors of a missing TOF detector.

C. Models

For the neural network for denoising and TOF detector reconstruction, we assess several neural network architectures: We train a CAE architecture with 5 hidden layers, which we refer to as CAE-64, with filter sizes 32, 64, 128, 256, 512, and in the bottleneck 64 for the encoder, similarly for the decoder but in reverse order. The filter has dimensions 3×3 , which is small enough to capture details but large enough to significantly reduce spatial dimensions. The stride is set to 2 to further reduce spatial dimensions. The padding is set to 1 to avoid underrepresentation of the border pixels. The output padding is set to 1 for a

better fit to the encoder dimensions. Finally, we add a bilinear upsampling layer for getting precisely the desired output shape of 60×16 , matching the simulation outputs: 16 TOF angles and 60 discrete, equidistant kinetic energy steps.

In addition, we assess alternative architectures with smaller or larger bottleneck dimensionality to provide the possibility of increasing the denoising level and decreasing reconstruction details. These architectures have filter sizes of 32, 128, 256, 512, and 1024 in the bottleneck. They replace the bottleneck layer with 64 filters from the CAE-64. This design choice reduces redundancy and inefficiency while mitigating the risk of vanishing gradients, which can occur when no significant transformations are performed. We refer to these architectures as CAE-32, CAE-128, CAE-256, CAE-512, and CAE-1024.

Due to the circular arrangement of the TOF detectors, the TOF detector at the most right in the simulation is adjacent to the most left TOF detector. We test the CCNNs described in Sec. II to model this occurrence. This extension replaces the zero padding in the convolution layers with circular padding. In circular padding, the left-side pixels are padded with values from the right-side edge of the input, and the right-side pixels are padded with values from the left-side edge.

We also tested U-Nets as presented in [19] with a similar structure as the CNN autoencoder architecture, but since these networks were overfitting quickly, we did not further investigate this approach.

As an activation function, the *Mish* function proposed in [20] outperformed the frequently used ReLU function. Furthermore, we used the AdamW optimizer as presented in [21]. The regularization term of the optimizer results in increased training and validation losses. However, the models denoise and reconstruct visually more accurately on real-world images, as shown in Appendix D. Thus, AdamW provides a countermeasure against overfitting on the simulation. We use learning rate plateau scheduling, beginning with a learning rate $\eta = 10^4$ and decaying it exponentially every epoch by multiplying it with 0.1 if the validation loss has not improved more than $\epsilon = 10^{-8}$ for three epochs. Despite the outputs being min-max normalized and thus between 0 and 1, using no activation function after the last layer resulted in slightly more accurate reconstruction and denoising than using a Sigmoid output function. We stopped the training after 50 epochs, since no significant increase in validation loss was noticeable. Using these best neural network parameters and architecture, we train the different models *1TOF*, *2TOF*, *3TOF*, *general* and *spec* with differently augmented data

as listed in Tab. II and compare those for different settings.

As baseline for the denoising process, we use a Wiener filter as described by Lim [22]. This Wiener filter works by minimizing the Mean Squared Error (MSE) between the estimated output signal and the original signal. It adapts its response based on both the signal and noise characteristics. We use a 3×3 filter window size, following our choice in the CAE. The noise is estimated as the average of the local variance – that refers to the variance in the corresponding filter window – of the input. The denoising process with Wiener filter is described more detailed in Appendix F.

D. Real-World Data Application

We use detector images from an experiment at LCLS as presented in [3] to show our method in a real-world setting. The time of flight t measured by the TOF spectrometers correlates with the energy E roughly proportional to $\text{const} + \frac{1}{t^2}$. Measurements are taken equidistantly in time of flight and then mapped onto equally sized energy intervals. Consequently, the number of measurement points in time of flight varies per equidistant energy E interval. This mapping is used because it is physically easier to measure equal intervals in terms of time of flight rather than energy. Furthermore, the scaling factors differ for all TOF detectors, and it would be required to remeasure and calculate the time-to-energy conversion for each experiment. Thus, it is easier to map the energies to equidistant 1 eV bins rather than adapting the simulation for every experiment.

Because of this binning of the energy values in 1 eV steps in the simulation, some bins always remain empty since, in the area with lower resolution, no TOF detector measures in the specific 1 eV range. To mitigate this issue, if a bin stays empty, we distribute a third of the values of the two neighboring bins to the empty bin. If an empty bin has only one neighbor, we shift half of the value of this bin to the empty one.

Furthermore, we round the positions of the TOF detectors scientifically. For example, the 280.5 eV TOF detector value is added to the 281 eV bin. After this procedure, we shift all negative TOF detector values to 0.0 and min-max normalize every detector image.

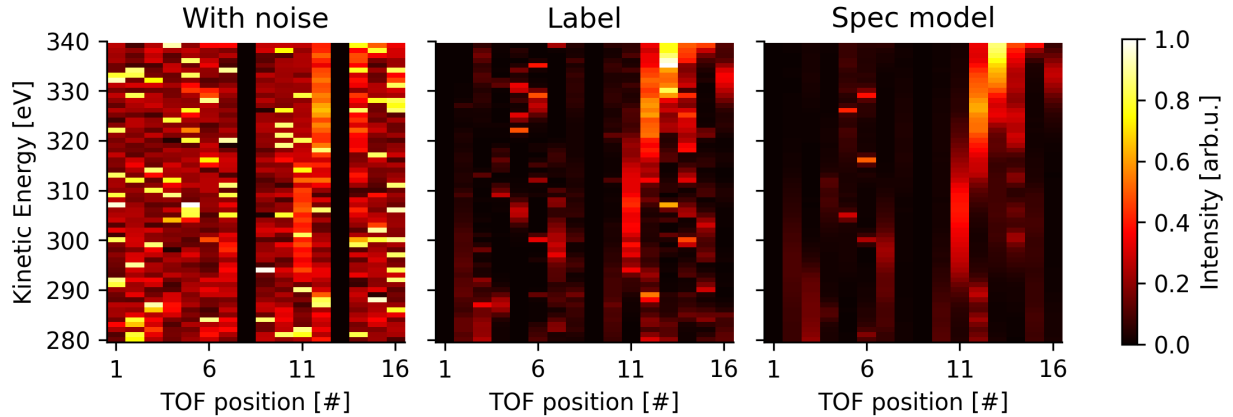


FIG. 2. The sample on the left is with two disabled TOF detectors, Gaussian noise and hot peaks. In the middle is the same sample without disabled TOF detectors and noise. The right plot shows the reconstructed and denoised detector image.

Failed TOFs	0
scenario	random
1TOF model	2.48e-3 †
2TOF model	3.10e-3 †
3TOF model	4.34e-3 †
General model	2.37e-3
Spec model	5.04e-3 †
Mean model	7.80e-2 †

TABLE III. RMSE on simulated data without failed TOF detectors for all models, showing model performance on only denoising.

IV. EVALUATION

In this section, we will first evaluate the denoising performance on detector images of our models. After that, we will examine the reconstruction of failed TOF detectors. For both applications, we will provide and discuss a real-world example.

Failed TOFs scenario	1	2	3	1-3	2	2	#8,#13
	random	random	random	random	neighbors	opposite	position
CAE-32	3.27e-3 †	3.42e-3 †	3.64e-3 †	3.47e-3 †	3.50e-3 †	3.37e-3 †	3.40e-3 †
CAE-64	2.48e-3 †	2.64e-3 †	2.85e-3 †	2.68e-3 †	2.72e-3 †	2.60e-3 †	2.60e-3 †
CAE-128	1.93e-3 †	2.10e-3 †	2.33e-3 †	2.14e-3 †	2.18e-3 †	2.06e-3 †	2.06e-3 †
CAE-256	1.54e-3 †	1.73e-3 †	1.97e-3 †	1.77e-3 †	1.80e-3 †	1.69e-3 †	1.72e-3 †
CAE-512	1.40e-3	1.63e-3	1.93e-3	1.68e-3	1.72e-3	1.59e-3	1.62e-3
Mean model	7.77e-2 †	7.76e-2 †	7.76e-2 †	7.77e-2 †	7.81e-2 †	7.72e-2 †	7.77e-2 †

TABLE IV. RMSE comparison across different architectures for different failure scenarios, with 1 to 3 TOF detectors disabled.

Failed TOFs scenario	1	2	3	1-3	2	2	#8,#13
	random	random	random	random	neighbors	opposite	position
1TOF model	2.48e-3	4.00e-3 †	6.61e-3 †	5.06e-3 †	6.72e-3 †	2.76e-3 †	2.74e-3 †
2TOF model	2.64e-3 †	2.67e-3 †	3.15e-3 †	2.90e-3 †	2.76e-3 †	2.63e-3 †	2.63e-3 †
3TOF model	3.17e-3 †	2.80e-3 †	2.86e-3	2.97e-3 †	2.87e-3 †	2.78e-3 †	2.74e-3 †
General model	2.48e-3	2.64e-3	2.86e-3	2.69e-3	2.72e-3	2.60e-3	2.60e-3 †
Spec model	9.99e-3 †	1.36e-2 †	1.68e-2 †	1.34e-2 †	1.35e-2 †	1.34e-2 †	2.40e-3
Mean model	7.76e-2 †	7.75e-2 †	7.76e-2 †	7.77e-2 †	7.81e-2 †	7.73e-2 †	7.78e-2 †

TABLE V. RMSE for different failure scenarios, where 1 to 3 TOF detectors are disabled.

A. Denoising

As shown in Tab. III, we compare the RMSE of different models. The scenario *0 failed* means that no TOF detector is disabled, thus the models perform only denoising. It is noticeable that the specifically trained models are worse in this scenario than the General model. Compared to the respectively best model, the baseline mean model is worse by almost a factor of 10 in terms of the RMSE. The † next to an RMSE value indicates a significant difference from the best models' RMSE. To assess whether differences in the RMSE values are meaningful, we compare the 99% Confidence Intervals (CIs) of the means and consider them significantly different if the CIs of this difference does not contain zero. Given the large test sample size of 600 000, we provide the CIs in Tab. VI to assess whether

the statistically significant differences are also practically relevant. Since the CIs are in the range of the RMSE values, we can consider the differences between the compared models and the Spec model practically relevant.

In Fig. 5 we show a comparison of the original real data and denoised with the model only trained on the scenario of failed TOF detectors #8 and #13. In Fig. 6 we deleted the data for two TOF detectors at positions #8 and #13 and used the model specifically trained to reconstruct the TOF detectors #8 and #13. We decided to show the results on this combination, since it contains one easier and one harder TOF detector to reconstruct, according to Fig. 3. We can see that the image, the model produces, is similar to the reconstruction of the detector image with all TOF detectors.

The RMSE between the Wiener filter output and the CAE-64 output is 0.143, while the RMSE between the original image and the CAE-64 output is 0.150. Additionally, the RMSE between the original images and the Wiener filter outputs is 0.072, which is significantly smaller compared to the differences with the CAE-64 outputs.

This shows that the CAE-64 output images are closer to the Wiener-filtered images than to the original images. However, the changes introduced by the Wiener filter are much smaller than those introduced by the CAE-64.

B. Reconstruction

In Fig. 2 we show an example of a noisy image from simulation with two disabled TOF detectors in the image on the left. We used the Spec model for denoising and reconstruction of the missing TOF detectors shown on the right image. The Spec model reconstructs most of the details in the label (center), while providing a fitting reconstruction of the missing TOF detectors. In Tab. IV we show the different architectures in terms of different sized bottlenecks. There is a clear connection between the bottleneck size and the reconstruction quality on synthetic data. The comparison of architectures with varying bottleneck sizes shows that larger bottlenecks result in more minor reconstruction errors in simulation data. The CAE-512 outperforms all other models in terms of the reached RMSE.

However, this behavior cannot be transferred to the real-world images: Larger bottlenecks exhibit weaker denoising performance when applied to real-world data, and the reconstructed TOF detector data integrate less cohesively with the rest of the detector image, as shown

in Fig. 6. Additionally, larger bottlenecks tend to reproduce noise peaks in the output. Conversely, smaller bottlenecks yield detector images closer in appearance to simulation data while being less detailed than the original real-world detector images. The outputs of the CAE-32 architecture tend to be overly simplistic, while larger bottlenecks allow for too many details, including noise artifacts. The CAE-64 balances reconstruction accuracy and effective denoising, making it the focus of this study. Nevertheless, other architectures may prove beneficial for different application scenarios.

In Tab. V, we quantitatively compare the models 1TOF, 2TOF, 3TOF with the general and mean model for different scenarios. In the *random* scenario, the number of disabled TOF detectors is drawn randomly from a uniform distribution. In the *neighbors* scenario, failures are introduced by disabling TOF detectors that are adjacent to each other. In the *opposite* scenario, opposing TOF detectors are disabled whenever possible. Finally, in the *position* scenario, TOF detectors at positions #8 and #13 are consistently disabled. The according general model performs significantly better than all other models, even if the model is trained for a more specialized scenario. The only exception is the 1TOF model for the scenario of one random TOF detector failure, but this difference is not statistically significant. The only exception is the scenario of the failure of TOF detectors at position #8 and #13, where the Specific model that is trained for failure of these specific positions performs significantly better. In Tab. IX we provide additional statistics with the CIs. The mean model is in all cases almost worse by a factor of 20 in comparison to the best model. In Fig. 3 we show the evaluation of the test dataset on the General model, i.e. 600 000 simulated examples. We evaluate the model with one missing TOF detector at all 16 possible positions and calculate the mean RMSE. We can see that the RMSE values of different TOF detector positions are pretty similar, but have slight peaks at position #6 and #14. This behavior arises because the angular distribution resulting from the chosen target gas leads to reduced intensity in this region, making it more challenging to predict. In Appendix E, we provide an additional, phase-separated examination of a single failed TOF detector.

In Fig. 4 we show a matrix of the evaluation of RMSE values for two failed TOF detectors. If a value is on the diagonal, we plot the RMSE value of the particular single failed TOF detector for reference. The darker the plot’s color, the lower the occurring RMSE. The highest error occurs if TOF detectors #13 and #14 fail, followed by #5 and #6 in a repeating pattern shifted by 8 TOF detectors. Generally, the combinations with TOF posi-

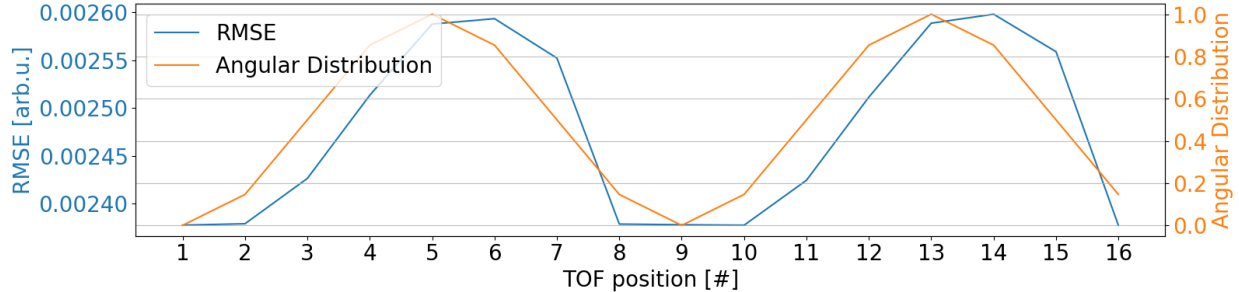


FIG. 3. The RMSE values of the reconstruction if one TOF detector has failed (blue). The y-axis is truncated for emphasizing the differences. For reference, we also plotted the angular distribution (orange).

tions #5, #6, #13, and #14 any other failed TOF detector have higher errors than the rest. This behavior also stems from the angular distribution of the experimental setup, similar to the single failed TOF detector examination. The best reconstructions are possible for combinations with TOF position #1, #2, #8, #9 and #16 have failed. This behavior can be explained since these TOFs detectors receive no electrons or only negligible amounts. Thus, these parts of the detector image can be reconstructed with smaller errors. The occurring patterns in reconstruction errors if two TOF detectors have failed fit to the patterns when one TOF detector has failed, as can be seen on the diagonal entries.

V. RESULTS & DISCUSSION

The evaluation in the previous section has shown that the models are able to accurately denoise and reconstruct 1–3 failed TOF detectors. We also tested the reconstruction of higher TOF detector counts, however the reconstruction quality decreases rapidly for 4 or 5 failed TOF detectors, as shown in Tab. X. We evaluated our models for several scenarios on an extensive test set that was not present during the training phase of the models.

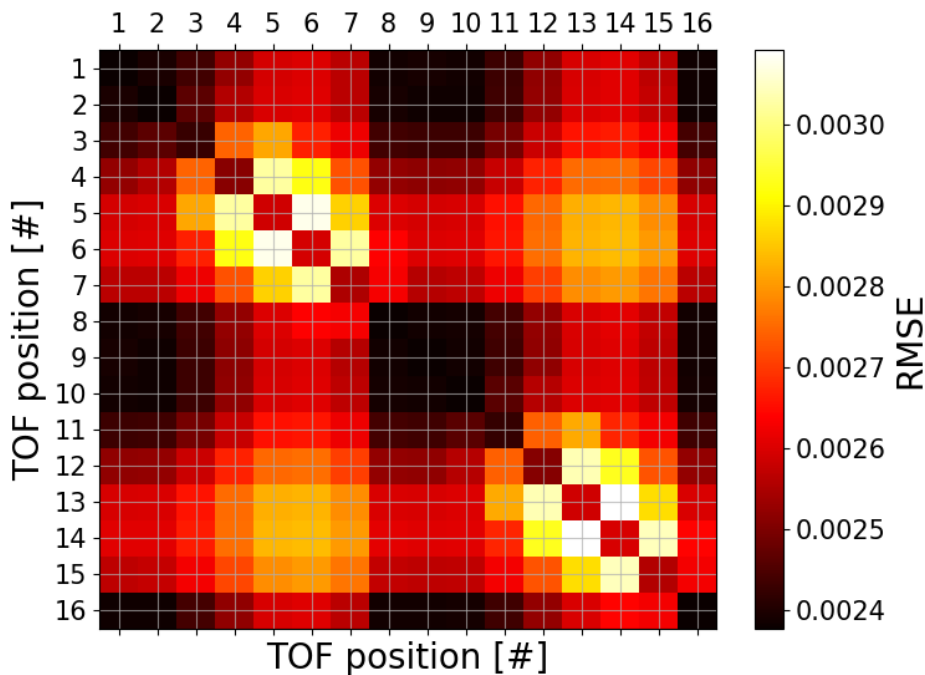


FIG. 4. The RMSE values of the reconstruction if two TOF detectors have failed.

The General model shows the best reconstruction quality if no TOF detectors have failed. This behavior is not surprising since no model was trained for that specific scenario, and due to its generality, this model is the most robust and thus can handle unseen cases the best. All presented neural network models reconstruct the missing TOF detectors considerably better than the baseline mean model. Furthermore, we have shown qualitatively that our models work on real-world images. The produced denoised detector images look similar to the noisy real-world images. If we additionally turn off TOF detectors on the real-world images, the model produces a similar image to a complete input detector image. A numerical evaluation for real-world images is impossible since we cannot generate noiseless detector images for comparison in a real-world scenario.

The comparison of the failure of one specific TOF detector shows that the position of a TOF has a considerable impact on its reconstruction loss, as shown in Fig. 3. A higher value in the angular distribution – that is due to the choice of the target gas and the experiment setup – means these areas often have lower intensities and more possible shapes. Also, combinations of neighbors and opposite TOF detectors result in the higher intensity regions of TOF detector positions #4-#7 and positions #12-#15 a slight increase in reconstruction

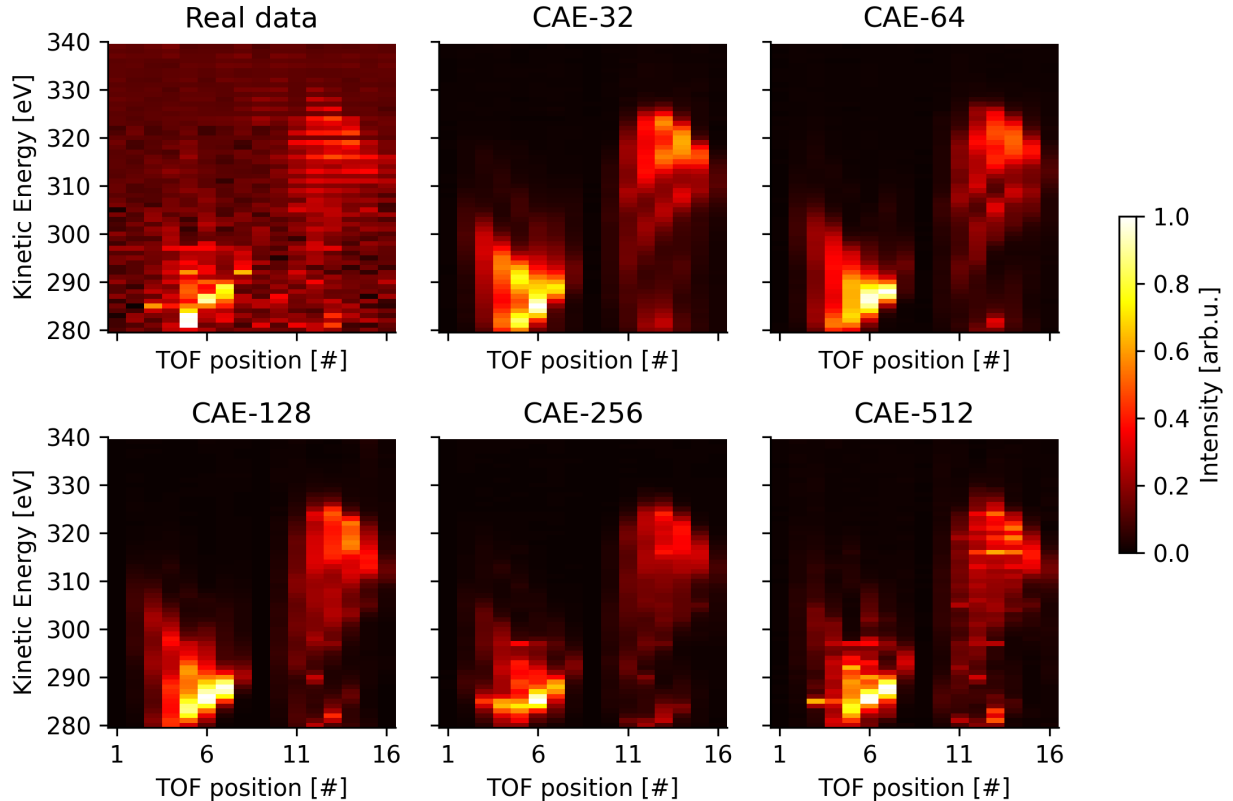


FIG. 5. The first plot shows a real-world detector image. The following plots show the denoised detector images across different-sized bottleneck model architectures. All models in these plots are trained in the general setting, that means with 1–3 TOF detectors disabled.

error. This phenomenon can be explained because neighboring or opposite TOF detectors share more information than other combinations. If both TOF detectors fail, more information is lost compared to other combinations. In the lower intensity regions of TOF detector positions #1-#3 and positions #8-#11 the differences in the reconstruction RMSE values are considerably less present. These aspects could be considered in future designs of angular streaking experiments.

Regarding neural network training, one of the essential things is regularization; we use the AdamW optimizer as described in [21]. This technique helps to keep the weights of the neural network low and thus avoids overfitting not only on training data but also on the simulation.

In Tab. VIII we show the evaluation of different neighboring factors γ . The ratio of shown training samples does not significantly change the training behavior since the RMSE

is almost equal for all scenarios. Since there is no adverse effect, we set $\gamma = 0.5$ for all subsequent experiments. We also tested the previously described CCNNs, which even decreased the reconstruction error. This behavior could be evoked by the cropping that is required in the transposed convolution layers in the decoder due to the additional paddings in the encoder part. Also the addition of padding to the input data decreases the reached RMSEs, this might happen because additional input comes to the cost of additional neurons that need to be learned.

The comparisons of the different models, the General model for 1–3 failed TOF detectors, and the models for the distinct number of failed TOF detectors show that the more specialized a model is, the more accurate its reconstructions are. However, we can verify this only for the simulated test data, even though the visual comparisons indicate similar results for the real-world samples. This behavior is probably caused by the more limited ranges of restored intensities in the case of more specialized scenarios. Thus, the trained model’s predictions are more accurate.

VI. CONCLUSION & OUTLOOK

The presented method provides online denoising and reconstruction of missing TOF detectors. We have shown that our presented approach for reconstructing missing TOF detectors outperforms a simple algorithm that calculates the mean over the remaining neighbors of a missing TOF detector. Validating our approach on real-world detector images is difficult because no labels exist. However, the results are visually viable, and due to its fast inference time, our presented method can be used during experimentation time for immediate monitoring and extraction of attributes for further pulse characterization. A first step towards this has been shown in [5]: Extracting the kick, Auger decay time, pulse structure, and duration is possible. The pulse structure is the intensity of a pulse over time, and the pulse duration is the period between a pulse’s first and last intensity. Complete and denoised data are inevitably required to obtain correct characterization results.

Alternative layouts for the angular streaking experiment can be efficiently tested and evaluated through simulation to optimize the design of experimental setups. These setups include configurations with higher overlapping TOF detector layouts or smaller TOF detectors, which correspond to smaller solid angles. A smaller solid angle refers to a reduced

portion of the detector’s field of view covered by each TOF detector, this can be compensated by increasing the number of detectors. Also, to test other scenarios or setups, the other simulation parameters can be changed, such as peak numbers or kick ranges. A realistic amount of noise can be added for all these scenarios, and the expected number of failed TOF detectors can be wiped and reconstructed. The error of denoising and reconstruction indicates if there is enough redundant information encoded so the detector image can be reconstructed.

The recently emerged diffusion models could be tested to improve our approach’s accuracy and robustness. However, this type of network typically requires at least 20 iterations for inference, which negatively impacts inference time, making them impracticable for an online evaluation setting. Nevertheless, a more accurate offline evaluation could benefit from applying diffusion models.

ACKNOWLEDGMENTS

Support by the JointLab AIM-ED between Helmholtz-Zentrum für Materialien und Energie, Berlin and the University of Kassel is gratefully acknowledged. We also acknowledge the useful feedback from the co-authors, Shang Gao and Pascal Plettenberg.

Appendix A: Evaluation Statistics

In this section we list the detailed statistics of the evaluated denoising and reconstruction scenarios for different models. The first number is the mean, followed by the standard deviation. In braces we supply the 99% CIs of the related t-test to check whether the differences of the RMSEs achieved by a model are statistically significant in comparison to the best evaluated model.

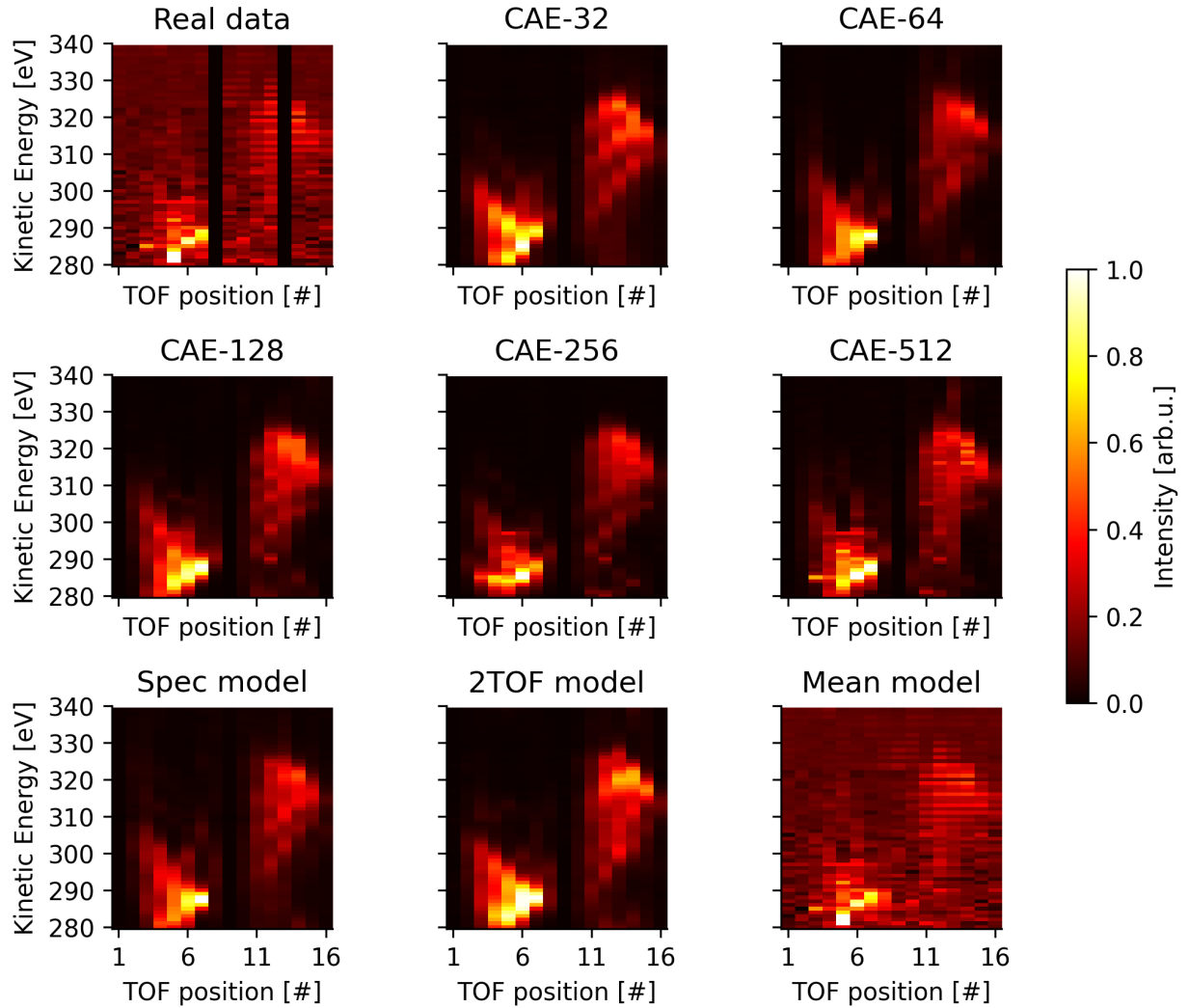


FIG. 6. The first plot shows a real-world detector image with two TOF disabled. The following plots show the denoised and reconstructed detector images across different model architectures. All models in these plots are trained in the general setting, that means with 1–3 TOF detectors disabled, except for the three models in the bottom line: The first one is the output of the CAE-64 model trained with data in spec setting (TOF positions #8 and #13 disabled, exactly the positions disabled for this reconstruction). The second one is the CAE-64 model trained with always two TOF detectors disabled. The last one is the output of the Mean model, that recreates the missing TOF sensors by averaging over its neighbors.

Failed TOFs scenario	0 random
1TOF model	$2.48\text{e-}3 \pm 2.08\text{e-}3$ (-1.08e-4, -9.84e-5)
2TOF model	$3.10\text{e-}3 \pm 3.18\text{e-}3$ (-7.42e-4, -7.05e-4)
3TOF model	$4.34\text{e-}3 \pm 1.12\text{e-}2$ (-2.06e-3, -1.88e-3)
General model	$2.37\text{e-}3 \pm 2.06\text{e-}3$
Spec model	$5.04\text{e-}3 \pm 2.74\text{e-}3$ (-2.68e-3, -2.65e-3)
Mean model	$7.80\text{e-}2 \pm 1.23\text{e-}2$ (-7.57e-2, -7.55e-2)

TABLE VI. Statistics for denoising scenario, where no TOF detectors are disabled.

Failed TOFs scenario	1	2	3	1-3	2	2	#8,#13
CAE-32	3.27e-3 $\pm 2.51e-3$ (-1.88e-3, -1.86e-3)	3.42e-3 $\pm 2.57e-3$ (-1.80e-3, -1.77e-3)	3.64e-3 $\pm 2.67e-3$ (-1.72e-3, -1.69e-3)	3.47e-3 $\pm 2.61e-3$ (-1.81e-3, -1.78e-3)	3.50e-3 $\pm 2.60e-3$ (-1.79e-3, -1.77e-3)	3.37e-3 $\pm 2.56e-3$ (-1.79e-3, -1.77e-3)	3.40e-3 $\pm 2.56e-3$ (-1.79e-3, -1.76e-3)
CAE-64	2.48e-3 $\pm 2.11e-3$ (-1.09e-3, -1.06e-3)	2.64e-3 $\pm 2.18e-3$ (-1.01e-3, -9.92e-4)	2.85e-3 $\pm 2.28e-3$ (-9.35e-4, -9.11e-4)	2.68e-3 $\pm 2.21e-3$ (-1.02e-3, -9.91e-4)	2.72e-3 $\pm 2.21e-3$ (-1.01e-3, -9.85e-4)	2.60e-3 $\pm 2.17e-3$ (-1.01e-3, -9.90e-4)	2.60e-3 $\pm 2.17e-3$ (-9.89e-4, -9.69e-4)
CAE-128	1.93e-3 $\pm 1.60e-3$ (-5.33e-4, -5.17e-4)	2.10e-3 $\pm 1.70e-3$ (-4.75e-4, -4.58e-4)	2.33e-3 $\pm 1.84e-3$ (-4.05e-4, -3.85e-4)	2.14e-3 $\pm 1.75e-3$ (-4.71e-4, -4.51e-4)	2.18e-3 $\pm 1.74e-3$ (-4.68e-4, -4.49e-4)	2.06e-3 $\pm 1.69e-3$ (-4.69e-4, -4.52e-4)	2.06e-3 $\pm 1.69e-3$ (-4.47e-4, -4.32e-4)
CAE-256	1.54e-3 $\pm 1.24e-3$ (-1.40e-4, -1.27e-4)	1.73e-3 $\pm 1.38e-3$ (-1.01e-4, -8.56e-5)	1.97e-3 $\pm 1.56e-3$ (-4.54e-5, -2.58e-5)	1.77e-3 $\pm 1.44e-3$ (-1.01e-4, -8.17e-5)	1.80e-3 $\pm 1.42e-3$ (-8.73e-5, -6.98e-5)	1.69e-3 $\pm 1.37e-3$ (-1.00e-4, -8.50e-5)	1.72e-3 $\pm 1.36e-3$ (-9.79e-5, -8.57e-5)
CAE-512	1.40e-3 $\pm 1.11e-3$	1.63e-3 $\pm 1.28e-3$	1.93e-3 $\pm 1.49e-3$	1.68e-3 $\pm 1.37e-3$	1.72e-3 $\pm 1.34e-3$	1.59e-3 $\pm 1.27e-3$	1.62e-3 $\pm 1.24e-3$
Mean model	7.77e-2 $\pm 1.23e-2$ (-7.64e-2, -7.62e-2)	7.76e-2 $\pm 1.22e-2$ (-7.60e-2, -7.58e-2)	7.76e-2 $\pm 1.22e-2$ (-7.58e-2, -7.56e-2)	7.77e-2 $\pm 1.22e-2$ (-7.62e-2, -7.60e-2)	7.81e-2 $\pm 1.21e-2$ (-7.64e-2, -7.62e-2)	7.72e-2 $\pm 1.23e-2$ (-7.57e-2, -7.55e-2)	7.77e-2 $\pm 1.22e-2$ (-7.62e-2, -7.60e-2)

TABLE VII. Statistics for reconstruction of different failure scenarios across different architectures, where 1 to 3 TOF detectors are disabled.

Failed TOFs scenario	1	2	3	1-3	2	2	#8,#13
$\gamma = 0.3$	2.50e-3	2.67e-3	2.89e-3	2.72e-3	2.76e-3	2.63e-3	2.62e-3
CAE-64	$\pm 2.11e-3$ (-3.28e-5, -2.44e-5)	$\pm 2.18e-3$ (-3.23e-5, -2.09e-5)	$\pm 2.28e-3$ (-4.30e-5, -2.73e-5)	$\pm 2.22e-3$ (-4.13e-5, -2.70e-5)	$\pm 2.21e-3$ (-4.32e-5, -3.00e-5)	$\pm 2.17e-3$ (-3.77e-5, -2.72e-5)	$\pm 2.16e-3$ (-2.41e-5, -1.62e-5)
$\gamma = 0.7$	2.51e-3	2.67e-3	2.89e-3	2.71e-3	2.75e-3	2.62e-3	2.63e-3
CAE-64	$\pm 2.10e-3$ (-3.57e-5, -2.72e-5)	$\pm 2.18e-3$ (-3.15e-5, -2.02e-5)	$\pm 2.28e-3$ (-3.94e-5, -2.38e-5)	$\pm 2.21e-3$ (-2.96e-5, -1.54e-5)	$\pm 2.21e-3$ (-3.16e-5, -1.84e-5)	$\pm 2.16e-3$ (-3.51e-5, -2.47e-5)	$\pm 2.16e-3$ (-2.79e-5, -2.00e-5)
$p = 0$	2.47e-3	2.64e-3	2.86e-3	2.69e-3	2.72e-3	2.59e-3	2.60e-3
CAE-64	$\pm 2.11e-3$	$\pm 2.18e-3$	$\pm 2.28e-3$	$\pm 2.22e-3$	$\pm 2.21e-3$	$\pm 2.16e-3$	$\pm 2.16e-3$
$p = 1$	2.52e-3	2.68e-3	2.92e-3	2.74e-3	2.78e-3	2.64e-3	2.65e-3
CAE-64	$\pm 2.11e-3$ (-4.53e-5, -3.70e-5)	$\pm 2.19e-3$ (-5.11e-5, -3.98e-5)	$\pm 2.30e-3$ (-6.75e-5, -5.16e-5)	$\pm 2.23e-3$ (-6.26e-5, -4.81e-5)	$\pm 2.22e-3$ (-6.11e-5, -4.78e-5)	$\pm 2.18e-3$ (-5.20e-5, -4.15e-5)	$\pm 2.18e-3$ (-5.00e-5, -4.21e-5)
$p = 2$	2.56e-3	2.73e-3	2.98e-3	2.79e-3	2.83e-3	2.69e-3	2.68e-3
CAE-64	$\pm 2.15e-3$ (-9.06e-5, -8.22e-5)	$\pm 2.22e-3$ (-9.56e-5, -8.42e-5)	$\pm 2.34e-3$ (-1.30e-4, -1.14e-4)	$\pm 2.27e-3$ (-1.09e-4, -9.41e-5)	$\pm 2.26e-3$ (-1.12e-4, -9.83e-5)	$\pm 2.22e-3$ (-9.76e-5, -8.70e-5)	$\pm 2.21e-3$ (-8.64e-5, -7.84e-5)
CCNN	2.49e-3	2.65e-3	2.87e-3	2.70e-3	2.73e-3	2.61e-3	2.61e-3
	$\pm 2.10e-3$ (-2.23e-5, -1.39e-5)	$\pm 2.17e-3$ (-1.52e-5, -3.96e-6)	$\pm 2.27e-3$ (-1.76e-5, -2.25e-6)	$\pm 2.21e-3$ (-2.12e-5, -7.04e-6)	$\pm 2.21e-3$ (-1.73e-5, -4.22e-6)	$\pm 2.16e-3$ (-2.09e-5, -1.04e-5)	$\pm 2.16e-3$ (-1.09e-5, -3.02e-6)

TABLE VIII. Statistics for reconstruction of different failure scenarios across different parameter settings, where 1 to 3 TOF detectors are disabled.

Failed TOFs scenario	1	2	3	1-3	2	2	#8,#13
	random	random	random	random	neighbors	opposite	position
1TOF model	2.48e-3 $\pm 2.07e-3$ (-4.82e-6, 4.28e-6)	4.00e-3 $\pm 4.05e-3$ (-1.40e-3, -1.34e-3)	6.61e-3 $\pm 6.46e-3$ (-3.81e-3, -3.70e-3)	5.06e-3 $\pm 5.63e-3$ (-2.42e-3, -2.33e-3)	6.72e-3 $\pm 5.67e-3$ (-4.04e-3, -3.95e-3)	2.76e-3 $\pm 2.19e-3$ (-1.66e-4, -1.54e-4)	2.74e-3 $\pm 2.17e-3$ (-3.48e-4, -3.37e-4)
2TOF model	2.64e-3 $\pm 2.22e-3$ (-1.73e-4, -1.61e-4)	2.67e-3 $\pm 2.18e-3$ (-4.14e-5, -3.00e-5)	3.15e-3 $\pm 2.57e-3$ (-3.11e-4, -2.85e-4)	2.90e-3 $\pm 2.48e-3$ (-2.28e-4, -2.05e-4)	2.76e-3 $\pm 2.21e-3$ (-4.41e-5, -3.08e-5)	2.63e-3 $\pm 2.17e-3$ (-3.56e-5, -2.51e-5)	2.63e-3 $\pm 2.16e-3$ (-2.33e-4, -2.24e-4)
3TOF model	3.17e-3 $\pm 5.34e-3$ (-7.36e-4, -6.57e-4)	2.80e-3 $\pm 2.34e-3$ (-1.74e-4, -1.58e-4)	2.86e-3 $\pm 2.28e-3$ (-1.48e-5, 1.39e-7)	2.97e-3 $\pm 3.07e-3$ (-3.01e-4, -2.65e-4)	2.87e-3 $\pm 2.31e-3$ (-1.57e-4, -1.42e-4)	2.78e-3 $\pm 2.32e-3$ (-1.94e-4, -1.79e-4)	2.74e-3 $\pm 2.32e-3$ (-3.48e-4, -3.33e-4)
General model	2.48e-3 $\pm 2.11e-3$	2.64e-3 $\pm 2.18e-3$	2.86e-3 $\pm 2.28e-3$	2.69e-3 $\pm 2.22e-3$	2.72e-3 $\pm 2.21e-3$	2.60e-3 $\pm 2.17e-3$	2.60e-3 $\pm 2.16e-3$ (-2.06e-4, -1.97e-4)
Spec model	9.99e-3 $\pm 7.11e-3$ (-7.58e-3, -7.45e-3)	1.36e-2 $\pm 8.64e-3$ (-1.10e-2, -1.09e-2)	1.68e-2 $\pm 9.50e-3$ (-1.40e-2, -1.38e-2)	1.34e-2 $\pm 9.22e-3$ (-1.08e-2, -1.06e-2)	1.35e-2 $\pm 8.77e-3$ (-1.09e-2, -1.07e-2)	1.34e-2 $\pm 9.13e-3$ (-1.09e-2, -1.08e-2)	2.40e-3 $\pm 2.00e-3$
Mean model	7.76e-2 $\pm 1.23e-2$ (-7.53e-2, -7.51e-2)	7.75e-2 $\pm 1.22e-2$ (-7.50e-2, -7.48e-2)	7.76e-2 $\pm 1.22e-2$ (-7.48e-2, -7.46e-2)	7.77e-2 $\pm 1.22e-2$ (-7.51e-2, -7.49e-2)	7.81e-2 $\pm 1.21e-2$ (-7.55e-2, -7.53e-2)	7.73e-2 $\pm 1.23e-2$ (-7.48e-2, -7.46e-2)	7.78e-2 $\pm 1.21e-2$ (-7.54e-2, -7.53e-2)

TABLE IX. Statistics for reconstruction of different failure scenarios, where 1 to 3 TOF detectors are disabled.

Failed TOFs scenario	4 random	5 random	1-4 random	1-5 random
CAE-64	$3.17\text{e-}3 \pm 2.46\text{e-}3$ (-6.40e-5, -4.28e-5)	$3.63\text{e-}3 \pm 2.79\text{e-}3$ (-2.03e-4, -1.72e-4)	$2.85\text{e-}3 \pm 2.33\text{e-}3$	$3.06\text{e-}3 \pm 2.55\text{e-}3$ (-6.98e-5, -4.31e-5)
1-4TOF	$3.14\text{e-}3 \pm 2.42\text{e-}3$ (-3.12e-5, -1.16e-5)	$3.50\text{e-}3 \pm 2.64\text{e-}3$ (-7.46e-5, -4.79e-5)	$2.86\text{e-}3 \pm 2.31\text{e-}3$ (-1.86e-5, 7.59e-7)	$3.03\text{e-}3 \pm 2.45\text{e-}3$ (-3.25e-5, -9.16e-6)
1-5TOF	$3.12\text{e-}3 \pm 2.41\text{e-}3$	$3.44\text{e-}3 \pm 2.59\text{e-}3$	$2.86\text{e-}3 \pm 2.31\text{e-}3$ (-2.09e-5, -1.87e-6)	$3.01\text{e-}3 \pm 2.42\text{e-}3$
Mean model	$7.77\text{e-}2 \pm 1.22\text{e-}2$ (-7.47e-2, -7.45e-2)	$7.82\text{e-}2 \pm 1.22\text{e-}2$ (-7.48e-2, -7.46e-2)	$7.79\text{e-}2 \pm 1.22\text{e-}2$ (-7.52e-2, -7.50e-2)	$7.81\text{e-}2 \pm 1.21\text{e-}2$ (-7.52e-2, -7.50e-2)

TABLE X. Statistics for reconstruction of different failure scenarios, where 4 or 5 TOF detectors are disabled.

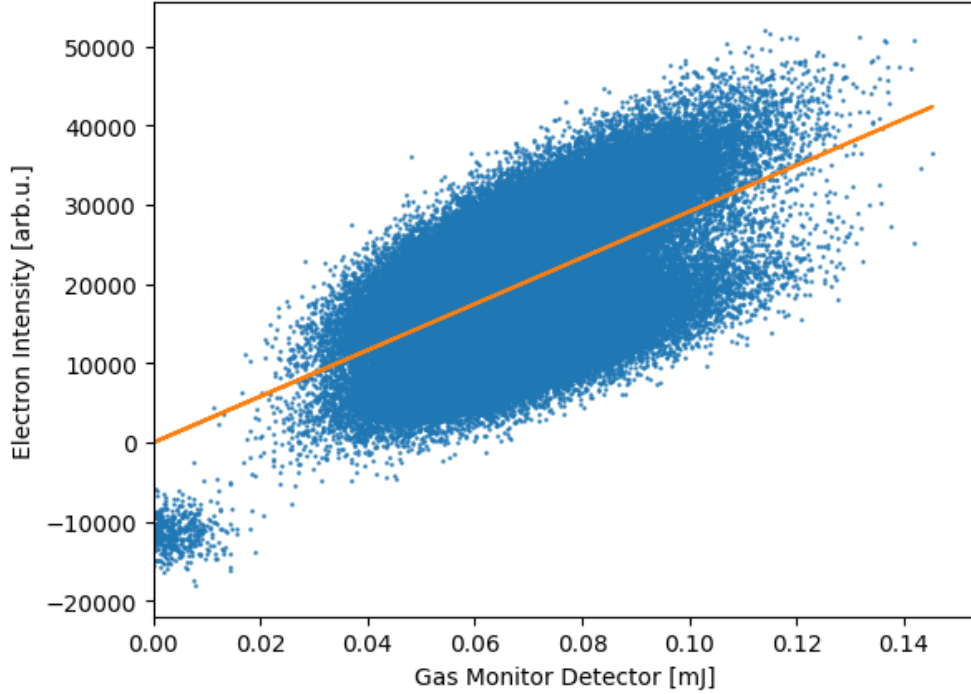


FIG. 7. Electron intensities vs. gas monitor detector values. The blue dots represent the measured data points, while the orange line is the linear approximation of these points. The plot is baseline corrected.

Appendix B: Checking for Saturation of TOF detectors

In this section, we compare the electron intensities measured by all TOF detectors with the outputs from the gas monitor detector. The gas monitor detector measures the calibrated ionization count, reflecting the overall ionization produced by the photons. As shown in Fig. 7, the blue data points in the plot remain linearly increasing in the higher regions of the gas monitor detector, closely following the linear approximation (orange line). This behavior suggests that the TOF detectors do not show saturation. For the calculation of the linear approximation, data points near $(0, 0)$ were excluded, as these correspond to shots recorded without lasing. For this scenario, both the gas monitor detector and the TOF detectors are uncalibrated and return values close to $(0, 0)$, making them unsuitable for reliable analysis. We corrected the baseline of the plot by shifting the linear fit to pass through the origin. Consequently, the data points were also adjusted to reflect this baseline correction.

Appendix C: TOF Detector Disablement Algorithm

Algorithm1 Algorithm for selecting random TOF detectors to disable, ensures to show samples with neighboring and opposite failed TOF detectors more often, as these constellations are harder to reconstruct.

```

1: procedure RANDOMTOFs( $n_{max}, \xi$ )  $\triangleright n_{max}$  is the maximum amount of TOFs to disable,  $\xi$  is
   the neighbor or opposite probability
2:    $l_{TOF} \leftarrow \pi([1, \dots, n_{TOF}])$   $\triangleright n_{TOF}$  is the total amount of TOFs,  $\pi$  is a random permutation
3:    $l_{disabled} \leftarrow [l_{TOF}[0]]$ 
4:    $n_{disabled} \sim \mathcal{U}(0, n_{max})$ 
5:   for  $i \in \{0, \dots, n_{disabled}\}$  do
6:      $r \sim \mathcal{U}(0, 1)$ 
7:     if  $r < \xi$  then
8:       if  $r < \frac{\xi}{2}$  then  $\triangleright$  Look for neighbor
9:         if for one element in  $l_{disabled}$  the left or right neighbor  $\eta$  is in  $l_{TOF}$  then
10:           AddItem( $l_{disabled}, \eta$ )
11:           RemoveItem( $l_{TOF}, \eta$ )
12:         else  $\triangleright$  If no neighbor, add a random element
13:           AddItem( $l_{disabled}, l_{TOF}[0]$ )
14:         end if
15:       else  $\triangleright$  Look for opposite
16:         if for one element in  $l_{disabled}$  the opposite  $\omega$  is in  $l_{TOF}$  then
17:           AddItem( $l_{disabled}, \omega$ )
18:           RemoveItem( $l_{TOF}, \omega$ )
19:         else  $\triangleright$  If no opposite, add a random element
20:           AddItem( $l_{disabled}, l_{TOF}[0]$ )
21:         end if
22:       end if
23:     end if
24:   end for
25:   return  $l_{disabled}$ 
26: end procedure

```

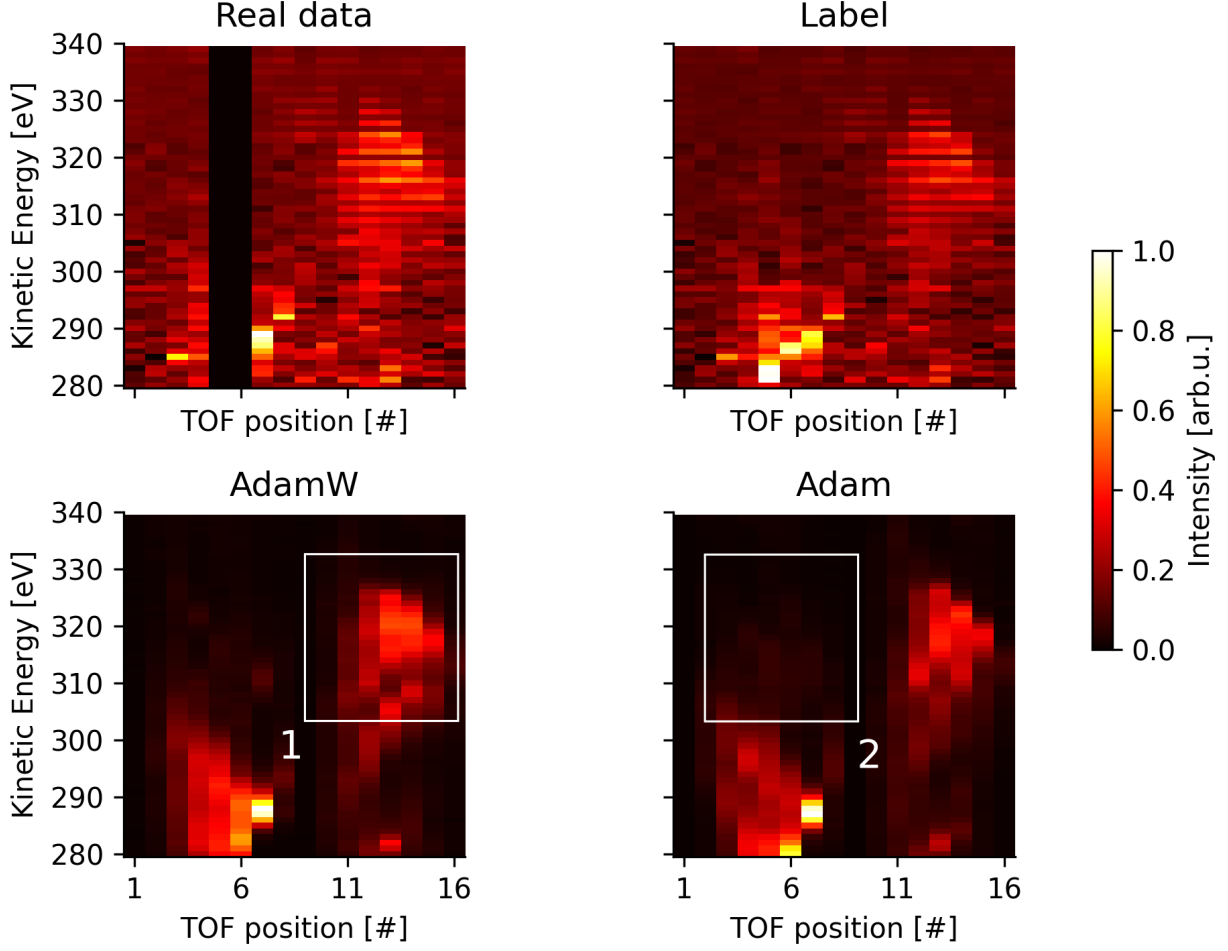


FIG. 8. Visual comparison of reconstruction performance between a network trained with AdamW (with regularization) and Adam (without regularization).

Appendix D: Impact of Regularization

As shown in Fig. 8, the AdamW-trained network reconstructs the broader intensity area more accurately (denoted with 1). In the region with minimal intensity in the label, the Adam-trained network reconstructs more incorrect intensity than the AdamW-trained network (2).

Appendix E: Phase-Separated Evaluation

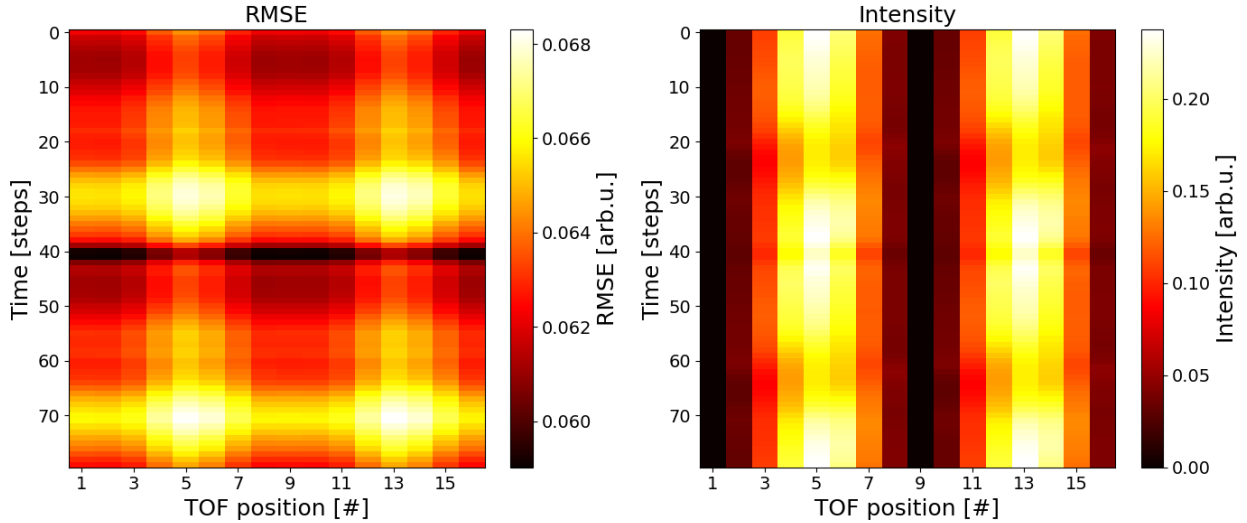


FIG. 9. Phase-resolved analysis of reconstruction quality. The left plot depicts the RMSE of the reconstruction for each phase step when a single TOF detector is disabled. The right plot shows the square root of the average intensities of 10,000 detector images across all phases and TOF positions.

In this section, we analyze the reconstruction quality across different phases. To achieve this, we generate 10 000 spectrograms spanning 80 phase steps, each with a single intensity peak at the corresponding phase and a random photon energy. Noise and other parameters are set accordingly to Sec. III. These spectrograms are then transformed into detector images for evaluation.

Using the General model, we assess the detector images by systematically deactivating one TOF detector at a time and calculating the RMSE of the resulting reconstructions. The results are presented in the left plot of Fig. 9, which shows that certain phases consistently exhibit lower reconstruction errors. For instance, phases around step 40 demonstrate higher reconstruction accuracy. This improvement arises because the maxima of the corresponding partial waves align with the maxima of the angular distribution, as illustrated in Fig. 3.

Contrary, specific combinations of phases and TOF detectors result in increased reconstruction errors. Especially phase steps 30 or 70, combined with a failure of TOF positions #5 or #13. These combinations lead to a significant loss of information regarding the relevant partial waves, thus degrading the reconstruction accuracy. For reference, we plotted the square root of the average intensities of all 10 000 detector images across all phases and TOF positions on the right side of Fig. 9.

Appendix F: Wiener Filter

The Wiener Filter in our used implementation by Virtanen *et al.* works by calculating the following steps [22, 23]:

1. Local Mean μ

$$\mu(x) = \frac{1}{|N|} \sum_{i \in N} I(x + i)$$

where I is the input detector image, N is in our case a $(3, 3)$ part from the entire detector image, referred to as window, $|N|$ is the total number of elements in the window N , and x represents the current pixel or element location.

2. Local Variance σ^2

$$\sigma^2(x) = \frac{1}{|N|} \sum_{i \in N} I(x + i)^2 - \mu(x)^2$$

3. Noise Power P_{noise}

The noise power is estimated as the mean of the local variances:

$$P_{\text{noise}} = \frac{1}{|X|} \sum_{x \in X} \sigma^2(x)$$

where $|X|$ is the total number of elements in I .

4. Filtered Output $O(x)$

Compute the Wiener filtered output:

$$O(x) = \begin{cases} \mu(x), & \text{if } \sigma^2(x) < P_{\text{noise}}, \\ \mu(x) + \left(1 - \frac{P_{\text{noise}}}{\sigma^2(x)}\right) \cdot (I(x) - \mu(x)), & \text{otherwise.} \end{cases}$$

This process is applied to every data point x in the input array I .

Appendix G: Data Availability

All dataset generation and program scripts to this article can be found at a repository hosted at Github: <https://github.com/hz-b/tof-reconstruction>.

- [1] W. Decking, S. Abeghyan, P. Abramian, A. Abramsky, A. Aguirre, C. Albrecht, P. Alou, M. Altarelli, P. Altmann, K. Amyan, V. Anashin, E. Apostolov, K. Appel, D. Auguste, V. Ayvazyan, S. Baark, F. Babies, N. Baboi, P. Bak, V. Balandin, R. Baldinger, B. Baranasic, S. Barbanotti, O. Belikov, V. Belokurov, L. Belova, V. Belyakov, S. Berry, M. Bertucci, B. Beutner, A. Block, M. Blöcher, T. Böckmann, C. Bohm, M. Böhnert, V. Bondar, E. Bondarchuk, M. Bonezzi, P. Borowiec, C. Bösch, U. Bösenberg, A. Bosotti, R. Böspflug, M. Bousonville, E. Boyd, Y. Bozhko, A. Brand, J. Branlard, S. Briechle, F. Brinker, S. Brinker, R. Brinkmann, S. Brockhauser, O. Brovko, H. Brück, A. Brüdgam, L. Butkowski, T. Büttner, J. Calero, E. Castro-Carballo, G. Cattalanotto, J. Charrier, J. Chen, A. Cherepenko, V. Cheskidov, M. Chiodini, A. Chong, S. Choroba, M. Chorowski, D. Churanov, W. Cichalewski, M. Clausen, W. Clement, C. Cloué, J. A. Cobos, N. Coppola, S. Cunis, K. Czuba, M. Czwalińska, B. D’Almagne, J. Dammann, H. Danared, A. de Zubiaurre Wagner, A. Delfs, T. Delfs, F. Dietrich, T. Dietrich, M. Dohlus, M. Dommach, A. Donat, X. Dong, N. Doynikov, M. Dressel, M. Duda, P. Duda, H. Eckoldt, W. Ehsan, J. Eidam, F. Eints, C. Engling, U. Englisch, A. Ermakov, K. Escherich, J. Eschke, E. Saldin, M. Faesing, A. Fallou, M. Felber, M. Fenger, B. Fernandes, J. M. Fernández, S. Feucker, K. Filippakopoulos, K. Floettmann, V. Fogel, M. Fontaine, A. Francés, I. F. Martin, W. Freund, T. Freyermuth, M. Friedland, L. Fröhlich, M. Fusetti, J. Fydrych, A. Gallas, O. García, L. Garcia-Tabares, G. Geloni, N. Gerasimova, C. Gerth, P. Geßler, V. Gharibyan, M. Gloor, J. Głowinkowski, A. Goessel, Z. Gołębiowski, N. Golubeva, W. Grabowski, W. Graeff, A. Grebentsov, M. Grecki, T. Grevsmuehl, M. Gross, U. Grosse-Wortmann, J. Grünert, S. Grunewald, P. Grzegory, G. Feng, H. Guler, G. Gusev, J. L. Gutierrez, L. Hagge, M. Hamberg, R. Hanneken, E. Harms, I. Hartl, A. Hauberg, S. Hauf, J. Hauschildt, J. Hauser, J. Havlicek, A. Hedqvist, N. Heidbrook, F. Hellberg, D. Henning, O. Hensler, T. Hermann, A. Hidvégi, M. Hierholzer, H. Hintz, F. Hoffmann, M. Hoffmann, M. Hoffmann, Y. Holler, M. Hüning, A. Ignatenko, M. Ilchen, A. Iluk, J. Iversen, J. Iversen,

M. Izquierdo, L. Jachmann, N. Jardon, U. Jastrow, K. Jensch, J. Jensen, M. Ježabek, M. Jidda, H. Jin, N. Johansson, R. Jonas, W. Kaabi, D. Kaefer, R. Kammering, H. Kapitzka, S. Karabekyan, S. Karstensen, K. Kasprzak, V. Katalev, D. Keese, B. Keil, M. Kholopov, M. Killenberger, B. Kitaev, Y. Klimchenko, R. Klos, L. Knebel, A. Koch, M. Koepke, S. Köhler, W. Köhler, N. Kohlstrunk, Z. Konopkova, A. Konstantinov, W. Kook, W. Koprek, M. Körfer, O. Korth, A. Kosarev, K. Kosiński, D. Kostin, Y. Kot, A. Kotarba, T. Kozak, V. Kozak, R. Kramert, M. Krasilnikov, A. Krasnov, B. Krause, L. Kravchuk, O. Krebs, R. Kretschmer, J. Kreutzkamp, O. Kröplin, K. Krzysik, G. Kube, H. Kuehn, N. Kujala, V. Kulikov, V. Kuzminych, D. La Civita, M. Lacroix, T. Lamb, A. Lancetov, M. Larsson, D. Le Pinvidic, S. Lederer, T. Lensch, D. Lenz, A. Leuschner, F. Levenhagen, Y. Li, J. Liebing, L. Lilje, T. Limberg, D. Lipka, B. List, J. Liu, S. Liu, B. Lorbeer, J. Lorkiewicz, H. H. Lu, F. Ludwig, K. Machau, W. Maciocha, C. Madec, C. Magueur, C. Maiano, I. Maksimova, K. Malcher, T. Maltezopoulos, E. Mamoshkina, B. Manschwetus, F. Marcellini, G. Marinkovic, T. Martinez, H. Martirosyan, W. Maschmann, M. Maslov, A. Matheisen, U. Mavric, J. Meißner, K. Meissner, M. Messerschmidt, N. Meyners, G. Michalski, P. Michelato, N. Mildner, M. Moe, F. Moglia, C. Mohr, S. Mohr, W. Möller, M. Mommerz, L. Monaco, C. Montiel, M. Moretti, I. Morozov, P. Morozov, D. Mross, J. Mueller, C. Müller, J. Müller, K. Müller, J. Munilla, A. Münnich, V. Muratov, O. Napoly, B. Näser, N. Nefedov, R. Neumann, R. Neumann, N. Ngada, D. Noelle, F. Obier, I. Okunev, J. A. Oliver, M. Omet, A. Oppelt, A. Ottmar, M. Oublaïd, C. Pagani, R. Paparella, V. Paramonov, C. Peitzmann, J. Penning, A. Perus, F. Peters, B. Petersen, A. Petrov, I. Petrov, S. Pfeiffer, J. Pflüger, S. Philipp, Y. Pienaud, P. Pierini, S. Pivovarov, M. Planas, E. Pławski, M. Pohl, J. Polinski, V. Popov, S. Prat, J. Prenting, G. Priebe, H. Pryschelski, K. Przygoda, E. Pyata, B. Racky, A. Rathjen, W. Ratuschni, S. Regnaud-Campderros, K. Rehlich, D. Reschke, C. Robson, J. Roever, M. Roggli, J. Rothenburg, E. Rusiński, R. Rybaniec, H. Sahling, M. Salmani, L. Samoylova, D. Sanzone, F. Saretzki, O. Sawlanski, J. Schaffran, H. Schlarb, M. Schlösser, V. Schlott, C. Schmidt, F. Schmidt-Foehre, M. Schmitz, M. Schmökel, T. Schnautz, E. Schneidmiller, M. Scholz, B. Schöneburg, J. Schultze, C. Schulz, A. Schwarz, J. Sekutowicz, D. Sellmann, E. Semenov, S. Serkez, D. Sertore, N. Shehzad, P. Shemarykin, L. Shi, M. Sienkiewicz, D. Sikora, M. Sikorski, A. Silenzi, C. Simon, W. Singer, X. Singer, H. Sinn, K. Sinram, N. Skvorodnev, P. Smirnow, T. Sommer, A. Sorokin, M. Stadler, M. Steckel, B. Steffen, N. Steinhau-Kühl, F. Stephan, M. Stodulski,

- M. Stolper, A. Sulimov, R. Susen, J. Świerblewski, C. Sydlo, E. Syresin, V. Sytchev, J. Szuba, N. Tesch, J. Thie, A. Thiebault, K. Tiedtke, D. Tischhauser, J. Tolkiehn, S. Tomin, F. Tonisch, F. Toral, I. Torbin, A. Trapp, D. Treyer, G. Trowitzsch, T. Trublet, T. Tschentscher, F. Ullrich, M. Vannoni, P. Varela, G. Varghese, G. Vashchenko, M. Vasic, C. Vazquez-Velez, A. Verguet, S. Vilcins-Czvitkovits, R. Villanueva, B. Visentin, M. Viti, E. Vogel, E. Volobuev, R. Wagner, N. Walker, T. Wamsat, H. Weddig, G. Weichert, H. Weise, R. Wenndorf, M. Werner, R. Wichmann, C. Wiebers, M. Wiencek, T. Wilksen, I. Will, L. Winkelmann, M. Winkowski, K. Wittenburg, A. Witzig, P. Wlk, T. Wohlenberg, M. Wojciechowski, F. Wolff-Fabris, G. Wrochna, K. Wrona, M. Yakopov, B. Yang, F. Yang, M. Yurkov, I. Zagorodnov, P. Zalden, A. Zavadtsev, D. Zavadtsev, A. Zhirnov, A. Zhukov, V. Ziemann, A. Zolotov, N. Zolotukhina, F. Zummack, and D. Zybin, A mhz-repetition-rate hard x-ray free-electron laser driven by a superconducting linear accelerator, *Nature Photonics* **14**, 391 (2020).
- [2] C. Bostedt, S. Boutet, D. M. Fritz, Z. Huang, H. J. Lee, H. T. Lemke, A. Robert, W. F. Schlotter, J. J. Turner, and G. J. Williams, Linac coherent light source: The first five years, *Rev. Mod. Phys.* **88**, 015007 (2016).
- [3] N. Hartmann, G. Hartmann, R. Heider, M. S. Wagner, M. Ilchen, J. Buck, A. O. Lindahl, C. Benko, J. Grünert, J. Krzywinski, J. Liu, A. A. Lutman, A. Marinelli, T. Maxwell, A. A. Miahnahri, S. P. Moeller, M. Planas, J. Robinson, A. K. Kazansky, N. M. Kabachnik, J. Viefhaus, T. Feurer, R. Kienberger, R. N. Coffee, and W. Helml, Attosecond time–energy structure of x-ray free-electron laser pulses, *Nature Photonics* **12**, 215 (2018).
- [4] U. S. Sainadh, H. Xu, X. Wang, A. Atia-Tul-Noor, W. C. Wallace, N. Douguet, A. Bray, I. Ivanov, K. Bartschat, A. Kheifets, R. T. Sang, and I. V. Litvinyuk, Attosecond angular streaking and tunnelling time in atomic hydrogen, *Nature* **568**, 75 (2019).
- [5] K. Dingel, T. Otto, L. Marder, L. Funke, A. Held, S. Savio, A. Hans, G. Hartmann, D. Meier, J. Viefhaus, B. Sick, A. Ehresmann, M. Ilchen, and W. Helml, Artificial intelligence for online characterization of ultrashort x-ray free-electron laser pulses, *Scientific Reports* **12**, 10.1038/s41598-022-21646-x (2022).
- [6] F. Bornemann and T. März, Fast image inpainting based on coherence transport, *Journal of Mathematical Imaging and Vision* **28**, 259 (2007).
- [7] H. Hukkelås, F. Lindseth, and R. Mester, Image inpainting with learnable feature imputation, in *Pattern Recognition*, edited by Z. Akata, A. Geiger, and T. Sattler (Springer International

- Publishing, Cham, 2021) pp. 388–403.
- [8] R. Köhler, C. Schuler, B. Schölkopf, and S. Harmeling, Mask-specific inpainting with deep neural networks, in *Pattern Recognition*, edited by X. Jiang, J. Hornegger, and R. Koch (Springer International Publishing, Cham, 2014) pp. 523–534.
- [9] J. Xie, L. Xu, and E. Chen, Image denoising and inpainting with deep neural networks, in *Proceedings of the 25th International Conference on Neural Information Processing Systems - Volume 1*, NIPS’12 (Curran Associates Inc., Red Hook, NY, USA, 2012) pp. 341–349.
- [10] G. Liu, F. A. Reda, K. J. Shih, T.-C. Wang, A. Tao, and B. Catanzaro, Image inpainting for irregular holes using partial convolutions, in *Computer Vision – ECCV 2018*, edited by V. Ferrari, M. Hebert, C. Sminchisescu, and Y. Weiss (Springer International Publishing, Cham, 2018) pp. 89–105.
- [11] C. Xie, S. Liu, C. Li, M.-M. Cheng, W. Zuo, X. Liu, S. Wen, and E. Ding, Image inpainting with learnable bidirectional attention maps, in *2019 IEEE / CVF International Conference on Computer Vision (ICCV)* (2019) pp. 8857–8866.
- [12] J. Yu, Z. Lin, J. Yang, X. Shen, X. Lu, and T. Huang, Free-form image inpainting with gated convolution, in *2019 IEEE / CVF International Conference on Computer Vision (ICCV)* (2019) pp. 4470–4479.
- [13] Y. Kossale, M. Airaj, and A. Darouichi, Mode collapse in generative adversarial networks: An overview, in *2022 8th International Conference on Optimization and Applications (ICOA)* (2022) pp. 1–6.
- [14] M. Arjovsky, S. Chintala, and L. Bottou, Wasserstein generative adversarial networks, in *Proceedings of the 34th International Conference on Machine Learning*, Proceedings of Machine Learning Research, Vol. 70, edited by D. Precup and Y. W. Teh (PMLR, 2017) pp. 214–223.
- [15] A. Lugmayr, M. Danelljan, A. Romero, F. Yu, R. Timofte, and L. Van Gool, Repaint: Inpainting using denoising diffusion probabilistic models, in *2022 IEEE/CVF Conference on Computer Vision and Pattern Recognition (CVPR)* (2022) pp. 11451–11461.
- [16] M. H. Givkashi, M. Hadipour, A. PariZanganeh, Z. Nabizadeh, N. Karimi, and S. Samavi, Image inpainting using autoencoder and guided selection of predicted pixels, in *2022 30th International Conference on Electrical Engineering (ICEE)* (2022) pp. 700–704.
- [17] S. Schubert, P. Neubert, J. Pöschmann, and P. Protzel, Circular convolutional neural networks for panoramic images and laser data, 2019 IEEE Intelligent Vehicles Symposium (IV) , 653

- (2019).
- [18] C. N. Yang, On the angular distribution in nuclear reactions and coincidence measurements, *Phys. Rev.* **74**, 764 (1948).
- [19] M. I. Hosen and M. B. Islam, Masked face inpainting through residual attention unet, in *2022 Innovations in Intelligent Systems and Applications Conference (ASYU)* (2022) pp. 1–5.
- [20] D. Misra, Mish: A self regularized nonmonotonic activation function (2020), arXiv:1908.08681 [cs.LG].
- [21] I. Loshchilov and F. Hutter, Decoupled weight decay regularization (2019), arXiv:1711.05101 [cs.LG].
- [22] J. Lim, *Two-dimensional Signal and Image Processing*, Prentice-Hall International Editions (Prentice Hall, 1990).
- [23] P. Virtanen, R. Gommers, T. E. Oliphant, M. Haberland, T. Reddy, D. Cournapeau, E. Burovski, P. Peterson, W. Weckesser, J. Bright, S. J. van der Walt, M. Brett, J. Wilson, K. J. Millman, N. Mayorov, A. R. J. Nelson, E. Jones, R. Kern, E. Larson, C. J. Carey, Í. Pólat, Y. Feng, E. W. Moore, J. VanderPlas, D. Laxalde, J. Perktold, R. Cimrman, I. Henriksen, E. A. Quintero, C. R. Harris, A. M. Archibald, A. H. Ribeiro, F. Pedregosa, P. van Mulbregt, and SciPy 1.0 Contributors, SciPy 1.0: Fundamental Algorithms for Scientific Computing in Python, *Nature Methods* **17**, 261 (2020).